



Biochemical and structural basis for the pharmacological inhibition of nuclear hormone receptor PPAR γ by inverse agonists

Received for publication, July 26, 2022, and in revised form, September 20, 2022. Published, Papers in Press, September 28, 2022.

<https://doi.org/10.1016/j.jbc.2022.102539>

Sean Irwin¹, Craig Karr¹, Craig Furman¹ , Jennifer Tsai¹, Patricia Gee¹, Deepti Banka¹, Ardian S. Wibowo² , Alexey A. Dementiev², Morgan O'Shea¹, Joyce Yang¹, Jason Lowe¹, Lorna Mitchell¹, Sabine Ruppel¹, Peter Fekkes¹, Ping Zhu¹, Manav Korpai¹, and Nicholas A. Larsen^{1,*}

From the ¹Department of Drug Discovery, H3 Biomedicine, Cambridge, Massachusetts, USA; ²Shamrock Structures, LLC, Illinois, USA

Edited by Wolfgang Peti

Recent studies have reported that the peroxisome proliferator-activated receptor gamma (PPAR γ) pathway is activated in approximately 40% of patients with muscle-invasive bladder cancer. This led us to investigate pharmacological repression of PPAR γ as a possible intervention strategy. Here, we characterize PPAR γ antagonists and inverse agonists and find that the former behave as silent ligands, whereas inverse agonists (T0070907 and SR10221) repress downstream PPAR γ target genes leading to growth inhibition in bladder cancer cell lines. To understand the mechanism, we determined the ternary crystal structure of PPAR γ bound to T0070907 and the corepressor (co-R) peptide NCOR1. The structure shows that the AF-2 helix 12 (H12) rearranges to bind inside the ligand-binding domain, where it forms stabilizing interactions with the compound. This dramatic movement in H12 unveils a large interface for co-R binding. In contrast, the crystal structure of PPAR γ bound to a SR10221 analog shows more subtle structural differences, where the compound binds and pushes H12 away from the ligand-binding domain to allow co-R binding. Interestingly, we found that both classes of compound promote recruitment of co-R proteins in biochemical assays but with distinct conformational changes in H12. We validate our structural models using both site-directed mutagenesis and chemical probes. Our findings offer new mechanistic insights into pharmacological modulation of PPAR γ signaling.

Urothelial cancer is the fifth most common cancer in the United States (1). The disease has a relatively favorable prognosis if diagnosed early, but approximately 30% of patients present at later stages with muscle-invasive bladder cancer (MIBC) and have a poorer prognosis if metastatic (2). Surgical resection followed by chemotherapy, if tolerated, has been the standard of care for these patients, yielding median overall survivals of 9 to 15 months (3). The recent approvals of immune checkpoint therapies have dramatically altered the treatment landscape with reported response rates of 15 to 20% (4). While this demonstrates remarkable progress, there is still a large segment of nonresponders, who would benefit from additional or complementary forms of therapy. Therefore, new precision medicines are urgently needed.

Analysis of The Cancer Genome Atlas reveals that MIBC has one of the highest somatic mutation burdens after lung cancer and melanoma (5–7). The majority of these patients (89%) carry inactivating mutations in tumor suppressors or cell cycle regulation genes, TP53, PTEN, or RB1 (4, 8, 9). The disease can be further divided into luminal or basal subtypes, according to their gene expression patterns (7). The luminal subtype has a more differentiated papillary morphology characterized by the expression of a number of distinctive uroplakin epithelial makers (10). The basal subtype is more invasive, with a squamous differentiation phenotype characterized by the expression of various keratin markers (10). Both subtypes respond to anti-PD-L1 therapy, with slightly higher response rates for the luminal subtype (11). Moreover, approximately 40% of MIBC tumors in The Cancer Genome Atlas show peroxisome proliferator-activated receptor gamma (PPAR γ) pathway activation mediated by focal amplification or overexpression of PPAR γ or recurrent hot spot mutations in RXR α , and this generally correlates with the luminal signature (12–14). PPAR γ pathway activation leads to the trans-repression of cytokines and is associated with a non-T-cell inflamed or immune-cold phenotype (12, 15). This observation could explain, at least in part, why some patients fail to respond to anti PD1/L1 therapy. Repression of PPAR γ signaling could therefore be a possible intervention strategy to

* For correspondence: Nicholas A. Larsen, nicka.larsen@gmail.com.

Present address for Jennifer Tsai: Monta Rosa Therapeutics, Boston, Massachusetts.

Present address for Ardian S. Wibowo: Helix Biostructures, Indianapolis, Indiana.

Present address for Alexey A. Dementiev: Schrodinger Inc, Natick, Massachusetts.

Present address for Morgan O'Shea: C4 Therapeutics, Watertown, Massachusetts.

Present address for Joyce Yang: Blueprint Medicines, Cambridge, Massachusetts.

Present address for Jason Lowe: Foghorn Therapeutics, Cambridge, Massachusetts.

Present address for Lorna Mitchell: Certa Therapeutics, Melbourne, Victoria, Australia.

Present address for Sabine Ruppel: Ikena Oncology, Boston, Massachusetts.

Present address for Peter Fekkes: 54 Gene, Washington, District of Columbia.

Inverse agonists inhibit PPAR γ through distinct mechanisms

reverse the immune-cold phenotype and improve anti-PD1/L1 response rates in these patients.

PPAR γ is type II nuclear hormone receptor (NHR) that contains a DNA-binding domain and a ligand-binding domain (LBD) and heterodimerizes with RXR α . When the LBD binds either synthetic agonists or natural unsaturated fatty acid ligands, the C-terminal helix (helix 12 [H12]) is stabilized in the agonist conformation, which permits recruitment of coactivator (co-A) complexes that trigger transcription of target genes responsible for metabolic homeostasis. Several such agonist compounds are clinically beneficial for their insulin-sensitizing effects in the treatment of type 2 diabetes (16). However, some of these agents also have potential association with increased risk of bladder cancer, leading to withdrawal in some markets (16). PPAR γ agonists also exhibit anti-inflammatory properties *via* transrepression of cytokines, consistent with the non-T-cell inflamed phenotype observed in PPAR γ^{high} tumors (17). In aggregate, the genetic and pharmacological data suggest that PPAR γ could be a relevant target in bladder cancer. Therefore, we set out to characterize pharmacological strategies for inhibiting PPAR γ in biochemical and cellular assays. Moreover, we sought to understand the structural basis for repression of PPAR γ signaling.

Results

Cancer-relevant mutations enhance co-A binding to PPAR γ

PPAR γ heterodimerizes with RXR α and together bind to DNA on PPAR response elements and recruit coregulator, either co-A or corepressor (co-R), complexes to set the basal transcription levels in the cell. Co-As and co-Rs usually bind PPAR γ in a mutually exclusive manner *via* conserved peptide motifs, LXXLL or LXXXIXXXI/L, respectively (18). The resulting protein–protein interface is relatively flat and contoured on one side by the C-terminal helix H12 of PPAR γ , which acts as a conformational switch that regulates coregulator recruitment (19). We first characterized PPAR γ interactions with representative co-A and co-R peptide motifs using isothermal titration calorimetry (ITC) and measured K_d 's in the low micromolar range, with co-A binding more favorably than co-R (Fig. 1A). Because binding equilibria are concentration dependent, PPAR γ basal transcriptional levels will reflect the relative expression levels of co-As and co-Rs and the relative levels of natural endogenous ligands in the cell. Therefore, the cellular context may dictate the basal transcriptional state of PPAR γ .

In certain bladder cancers, mutations in RXR α or PPAR γ can activate basal transcriptional levels (12, 13, 20). The recurring RXR α^{S427F} mutation has at least four mechanistic consequences. First, the mutation shifts the RXR α equilibrium from an inactive homotetramer to the active monomer (12). Second, the mutation stabilizes the dimer interface between RXR α and PPAR γ (12), and third, F427 stacks with PPAR γ Y505, which stabilizes helix H12 of PPAR γ in the active conformation (11). This stabilization of H12 enhances the binding to co-A and is similar to that observed in the estrogen receptor alpha harboring the activating Y537S hot spot

mutation (Fig. 1A). In both cases, stabilization of H12 enhances binding to co-As by preordering the co-A binding site (Fig. 1A). Finally, because the S427F mutation shifts the equilibrium to the agonist conformation, binding to co-R becomes less favored (Fig. 1A). The crystal structure of another activating PPAR γ^{T475M} mutation complex with agonist also shows stabilizing interactions occurring between M475 and the C-terminal Y505, resulting in overall H12 stabilization in the agonist conformation and activated PPAR γ -mediated transcriptional levels in the cell (20). These examples demonstrate that PPAR γ is a key signaling pathway for certain cancers. More broadly, these biophysical data highlight the selective pressure in the tumor that converges mechanistically on stabilization of helix H12 to activate downstream signaling for different NHRs.

Pharmacological modulation of PPAR γ

In addition to these disease-relevant mutations, the basal transcriptional levels can be activated or repressed by agonist or inverse agonist ligands, respectively (Fig. 1B) (13). One of the best known agonists is rosiglitazone (Fig. 1C), an approved drug, used as an insulin sensitizer for the treatment of type 2 diabetes. Many other agonists have been reported and extensively reviewed (16). In contrast, there are only a handful of inverse agonists described in the literature: T0070907 (T007) (21), the related compound JTP-426467 (JTP-4) (22), and the chemically distinct SR10221 (23) (Fig. 1C). Both T007 and JTP-4 are covalent compounds that modify C313 in the ligand-binding pocket of PPAR γ , whereas SR10221 binds non-covalently. The modified cysteine is the same one that covalently engages endogenous fatty acid ligands, further highlighting the importance of this residue (24).

In order to determine which co-As and co-Rs would respond to agonists *versus* inverse agonists, we developed a binding assay using an array of peptides representing the known binding motifs in coregulators. Comparison of the agonist rosiglitazone and the inverse agonists T007 and SR10221 reveals opposite profiles where rosiglitazone only promotes binding to co-A peptides, whereas the inverse agonists only promote binding to co-R peptides (Fig. 1D). We hypothesized that this enhancement in FRET signal was due to stronger binding to the peptides. To confirm this, we performed a series of ITC experiments. First, we determined the K_d 's for compound alone (SR10221 and T007) (Figs. 1E and S1), and then we loaded PPAR γ with ligand and performed titrations using the co-R peptide (Fig. 1, E and F). These data clearly show at least a sixfold enhancement of binding to the co-R motif in the presence of inverse agonist.

Guided by our biophysical insight into these interactions, we developed several high-throughput time-resolved (TR)-FRET assays to support compound characterization (Figs. 2A and S2). In these assays, a terbium-labeled anti-His $_6$ antibody acts as an FRET donor, which binds to a His $_6$ tag on the amino terminus of PPAR γ , and a fluorescently labeled co-A or co-R peptide is the FRET acceptor. TR-FRET signal is observed, in a ligand concentration–dependent manner, upon peptide

Inverse agonists inhibit PPAR γ through distinct mechanisms

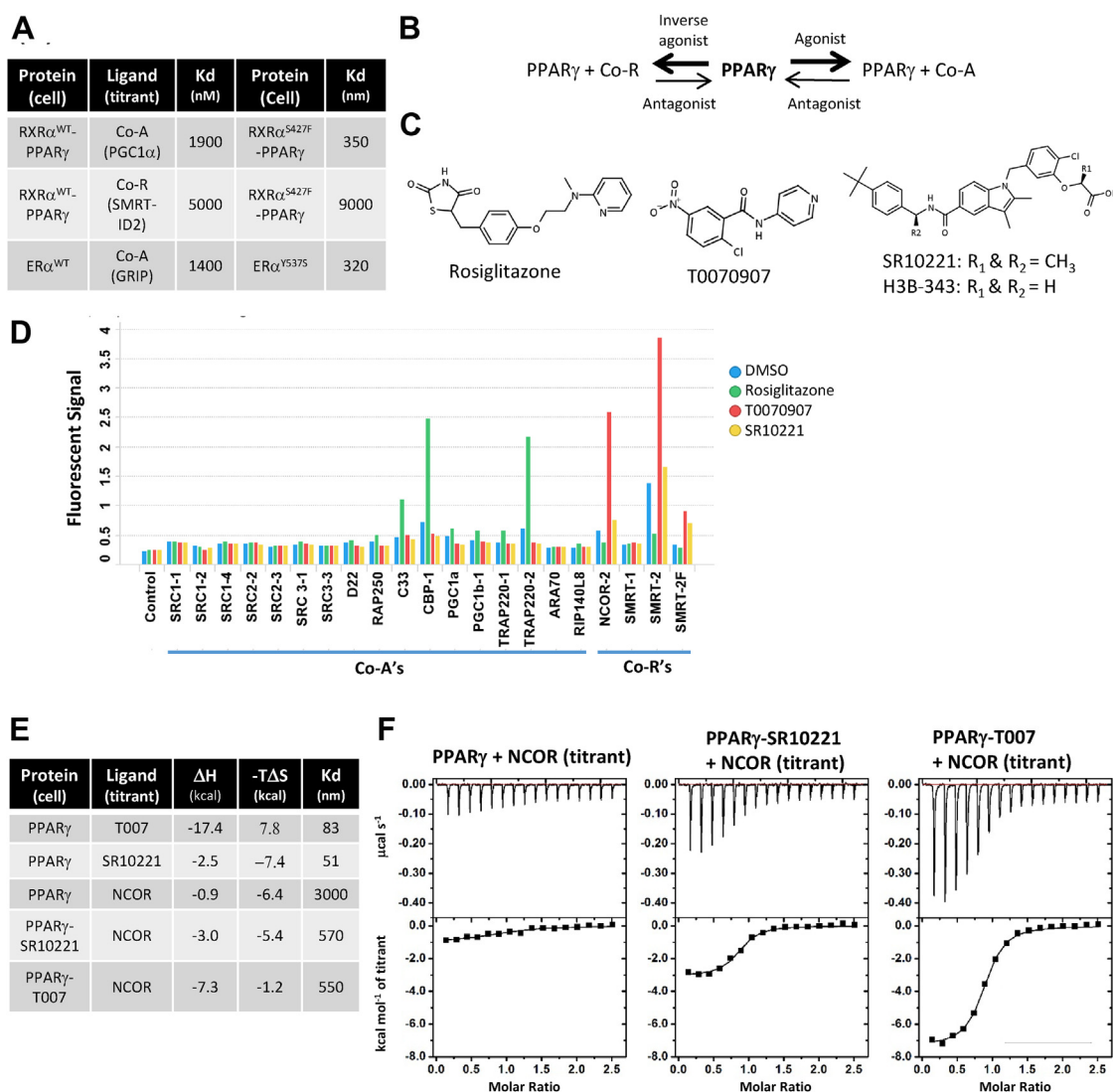


Figure 1. Inverse agonists enhance binding of PPAR γ to corepressors. A, PPAR γ binds co-A and co-R in the absence of ligand. Binding is enhanced to co-A and reduced to co-R in the mutant setting. The disease relevant mutation in ER α shows a similar trend. B, model for inverse agonism. C, examples of reported agonist and inverse agonists. D, agonists and inverse agonists qualitatively enhance binding to co-A and co-R peptides in a TR-FRET binding assay ($n = 1$). E, summary of ITC data with inverse agonists and co-R peptide. F, ITC data demonstrating enhanced binding to co-R in the presence of inverse agonist compounds. co-A, coactivator; co-R, corepressor; ITC, isothermal titration calorimetry; PPAR γ , peroxisome proliferator-activated receptor gamma; TR-FRET, time-resolved FRET.

recruitment to form the ternary complex (Fig. 2A). Our assay clearly demonstrates that rosiglitazone only promotes binding of co-A (agonist profile), whereas T007 only promotes binding to co-R (inverse agonist profile) (Fig. 2A). In these assays, the FRET signal is normalized to controls containing 1 μ M rosiglitazone or 0.5 μ M T007. The inflection point of the curve indicates the affinity of the ligand for receptor, and the amplitude is a qualitative gauge for the affinity of the peptide for the receptor in the presence of ligand. Conceptually, assuming no other sources of assay artifact, maximal FRET response (R_{max}) values less than 100% reflect weaker binding to peptide (partial agonism or inverse agonism), and values greater than 100% show stronger peptide binding (super agonists or inverse agonists).

In addition to these functional assays, we also developed a TR-FRET-based fluormone binding assay to provide additional

confidence that our compounds engage the LBD. In this assay, we use the same TR-FRET donor but now use fluormone, a known fluorescent PPAR γ ligand, as the FRET acceptor. This assay directly monitors fluormone displacement, irrespective of the modulatory behavior on H12 and peptide recruitment. Because compound directly competes with fluormone leading to its displacement, there is no variation in curve amplitude as observed in the peptide recruitment assays. As expected, both rosiglitazone and T007 compete with fluormone leading to loss of FRET signal (Fig. 2A). Therefore, from these three simple assays, we are able to classify compounds amidst the continuum of agonist and inverse agonist profiles and, from these analyses, distinguish a third class of modulators as pure antagonists. In these assays, an antagonist is defined as a compound that binds to PPAR γ (completely displaces fluormone) but does not influence recruitment of co-A or co-R. In

Inverse agonists inhibit PPAR γ through distinct mechanisms

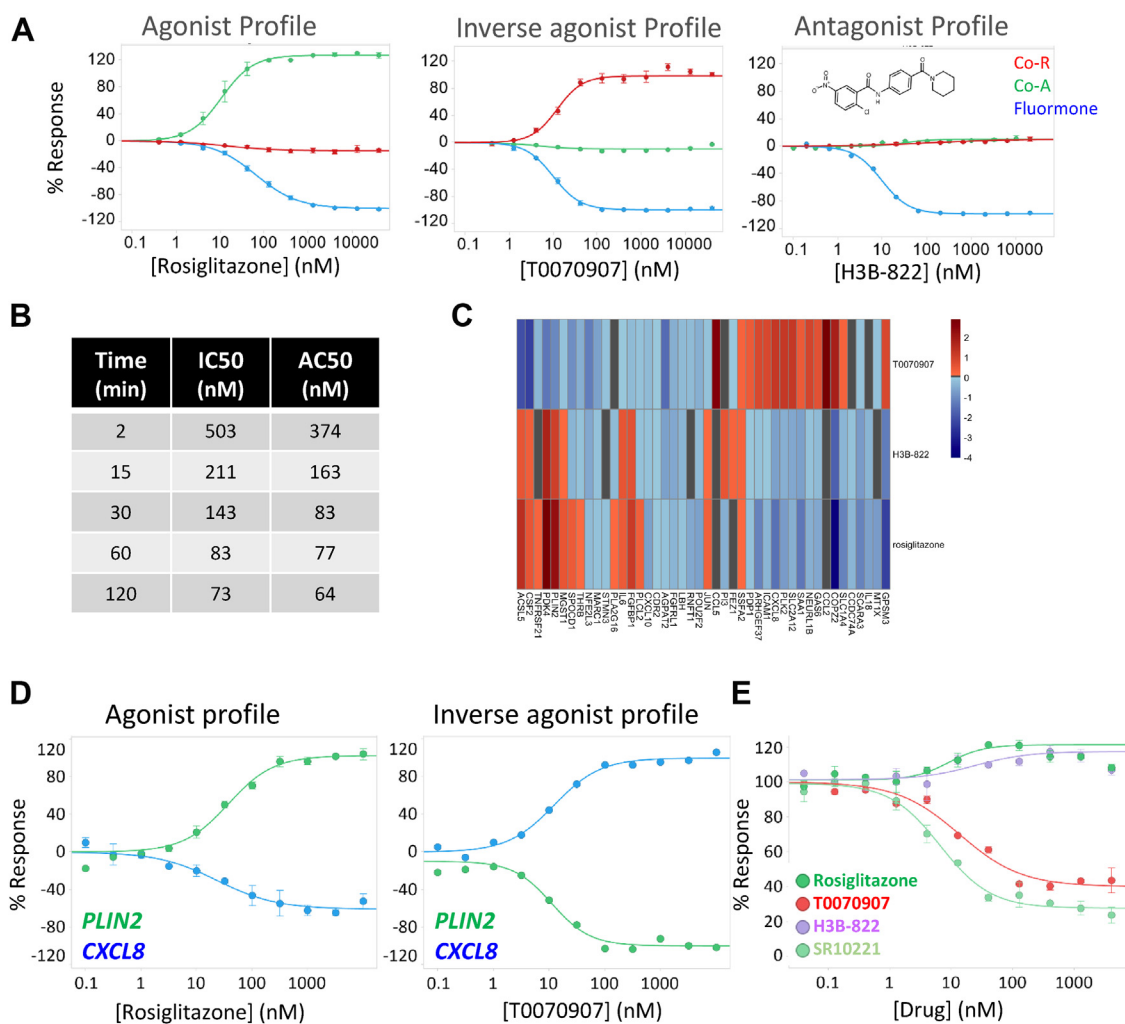


Figure 2. Biochemical and cellular profile of inverse agonists. *A*, high-throughput FRET assays ($n = 3$) showing agonists recruit co-A and inverse agonists recruit co-R, whereas antagonists recruit neither. All three classes of compounds compete with fluormone binding. *B*, T007-like compounds (e.g., JTP-4) are covalent, and IC₅₀ and AC₅₀ values show a qualitative time-dependent shift ($n = 1$). *C*, nanostring data from 5637 cells showing gene expression profiles after treatment with agonist, inverse agonist, and antagonist. The antagonist is more similar to DMSO or a weak partial agonist. The heat map is shown on a Log₂ scale. *D*, qPCR showing activity of rosiglitazone and T007 in UM-UC-9 cells ($n = 2$). *E*, viability assays in UM-UC-9 cells ($n = 2$). Agonists have modest stimulatory effect, whereas inverse agonists show growth inhibition. %Response normalization is done such that zero on the y-axis represents stasis and -100 represents lethality. co-A, coactivator; co-R, corepressor; qPCR, quantitative PCR; T007, T0070907.

the course of our compound profiling, we identified several “pure” antagonists from both the T007 and the SR10221 series (Figs. 2*A* and S2).

We next set out to further characterize the known inverse agonists T007 and SR10221. The most obvious difference in their mechanism of action is covalency (21). NMR studies have shown that T007 induces slow conformational changes (25). We therefore performed a FRET-based time course to examine if the IC₅₀ in our fluormone assay and AC₅₀ in our co-R recruitment assay would show time dependence. By changing the preincubation time with the compound, we observe a clear time-dependent shift in the activity of the T007-related compound JTP-4, consistent with the NMR data and covalent mechanism of action (Fig. 2*B*). Based on these data, we selected 1 h as an appropriate preincubation time of protein with compound to allow for equilibrium and followed this time point strictly to avoid time-dependent drift in IC₅₀ and AC₅₀ measurements for covalent compounds.

Our previous work and that of others demonstrated that suppression of PPAR γ signaling could be a useful therapeutic axis in bladder cancer (12, 13). One of the key questions has been concerned with the modality of suppression, whether antagonism or inverse agonism is required. To address this, we analyzed an agonist, antagonist, and inverse agonist in a nanostring panel comprised of PPAR γ -dependent genes (Fig. 2*C*). For this nanostring experiment, we used the 5637 bladder cancer cell line that has modest upregulation of PPAR γ (12, 13). These data clearly show that whereas the antagonist H3B-822 results in partial agonism, the inverse agonist T007 effectively suppresses PPAR γ activity. These data support inverse agonists as the necessary modality for suppressing PPAR γ signaling in the cellular setting.

From the nanostring panel, we selected two genes, *PLIN2*, which is positively regulated by PPAR γ , and *CXCL8*, which is negatively regulated, for additional quantitative PCR (qPCR) analysis (Figs. 2*D* and S3) in the UM-UC-9 PPAR γ^{high} bladder

cancer cell line. These genes show robust changes upon compound treatment, and this assay allows for convenient compound profiling. Like the TR-FRET assays described previously, the amplitude is normalized to positive control rosiglitazone for the agonist signal and SR10221 for the inverse agonist. The IC_{50} or AC_{50} of the curve is a metric for the cellular compound potency to PPAR γ , and the amplitude of the curve reflects either partial or super (inverse) agonism relative to controls. These qPCR data confirm that the expression of *PLIN2* and *CXCL8* is inversely correlated to each other and is stimulated or repressed by agonist and inverse agonist treatment, respectively (Fig. 2D). In contrast, the compounds that show antagonism in the FRET assays are inactive or weak partial agonists in the qPCR assays (Figs. S2 and S3).

Given the pharmacodynamic modulation at the pathway level, we then profiled the compounds in CellTiter-Glo (Promega) viability assays using bladder cancer cell lines. For this, we chose two cell lines, one with high levels of PPAR γ expression (UM-UC-9) and one with low levels of PPAR γ expression (UM-UC-3) (13). Our data indicate a clear growth-inhibitory phenotype in UM-UC-9 but not in UM-UC-3, and this phenotype is only apparent for the inverse agonists and not the antagonists (Fig. S4), in line with the previous report (13). Taken in total, these nanostring, qPCR, and viability data clearly demonstrate that inverse agonism is the appropriate therapeutic modality for PPAR γ inhibition in the cellular setting. To suppress the PPAR γ pathway, it is not sufficient to use an antagonist that merely binds PPAR γ . Rather, effective pathway suppression also requires recruitment of co-R complexes in addition to suppression in co-A recruitment.

Crystal structures from the SR10221 series and implications for inverse agonism

To better understand the mechanism underpinning co-R recruitment by these inverse agonists, we endeavored to determine their crystal structures. The most common crystal form for PPAR γ derives from a citrate condition and shows PPAR γ as a homodimer with two monomers in the asymmetric unit (Fig. S5) (26). In this crystal form, both monomers are similar except for the conformation of the C-terminal helix H12. In one monomer, H12 adopts an “in” conformation closely resembling the agonist state, whereas in the other, H12 has an “out” conformation incompatible with co-A binding. This “out” conformation is stabilized by crystal packing interactions with the co-A binding site from a neighboring monomer in the lattice (Fig. S5). This H12, therefore, mimics a co-A peptide by domain swapping with the co-A binding site of a neighboring monomer in the lattice (Fig. S5). Thus, the two monomers represent two conformational states of PPAR γ . One state is the agonist conformation, whereas the other is incompatible with co-A binding.

A closer examination of the agonist conformation reveals interactions critical for stabilizing H12, necessary for co-A binding (Fig. 3, A–C). These include Q314 from helix 3 (H3), which forms H-bond interactions with the backbone of

helix H12, as well as H351 and H477, which form H-bond and π – π stacking interactions with Y501. Together, these help stabilize H12 in the agonist conformation (Fig. 3B). Comparison with the rosiglitazone and co-A-bound crystal structure shows how these residues, Q314, H351, H477, and Y501, interact with the compound and further stabilize H12 in the agonist conformation to facilitate co-A binding (Fig. 3C). Here, H12 presents E499 in the co-A binding site where it forms critical H-bond interactions with the backbone amides from the first helical turn of the co-A peptide, allowing for robust recruitment of co-A (Fig. 3C). This explains why agonists do not recruit co-R because this conformation of H12 cannot accommodate the extra helical turn in co-R motif. In order for co-R to bind, H12 needs to be displaced.

To characterize this displacement mechanism, we first endeavored to obtain crystal structures with SR10221 or representative crystal structures from this series (Fig. 3, D–F). First, we noted that SR10221 has two stereogenic methyl groups in the (S, S) configuration. Interestingly, when the stereochemistry is reversed to (R, R), the resulting compound, H3B-487, shows partial agonist and weak partial inverse agonist activities in the FRET biochemical assays (Table 1, Figs. S2I and S3B). In the cellular qPCR assay, the compound behaves as a partial agonist with roughly half the overall response as rosiglitazone (Fig. S3B). From the cellular data, therefore, H3B-487 may be classified as a partial agonist, which is the opposite profile of SR10221. To understand how H3B-487 could have such different modulatory behavior, we first determined the crystal structure with H3B-487 at 2.48 Å resolution, using the citrate condition previously described, and observed clear electron density for the ligand (Figs. 3E and S6A). The compound wraps around H3 with the indole core right above C313 and the acid extending back toward S330. The amide forms an H-bond to S317, whereas the *t*-butyl-phenyl group is directed toward H12. Interestingly, the *t*-butyl-phenyl group shows different conformations in the two monomers of the asymmetric unit (Fig. S7A). When H12 is in the agonist conformation, this moiety is flipped back toward Q314, where it maintains its H-bonding interaction to H12 (Fig. 3E). In this pose, Y501 remains anchored in place by H351 and H477, thus stabilizing H12 in its agonist conformation (Fig. 3E). In the other monomer, the *t*-butyl-phenyl is flipped 90° and would be disruptive to the agonist conformation (Fig. S7A). We speculated that this second pose could be representative of the inverse agonist conformation. This mixed binding mode might explain why we observe both partial agonist and partial inverse agonist activity in the FRET biochemical assays, although the cellular induction of *PLIN2* suggests the overall equilibrium is in agonist state (Table 1).

Given these insights, we then sought to obtain cocrystals with the inverse agonist SR10221 with the (S,S) configuration. Our crystallization efforts were unsuccessful, and we failed to obtain cocrystals with it and the co-R peptide. However, we noted in our compound profiling efforts that the non-stereogenic analog H3B-343 was equipotent to SR10221 in biochemical and qPCR assays (Table 1, Figs. S2H and S3B). We were able to obtain cocrystals of PPAR γ with H3B-343 at

Inverse agonists inhibit PPAR γ through distinct mechanisms

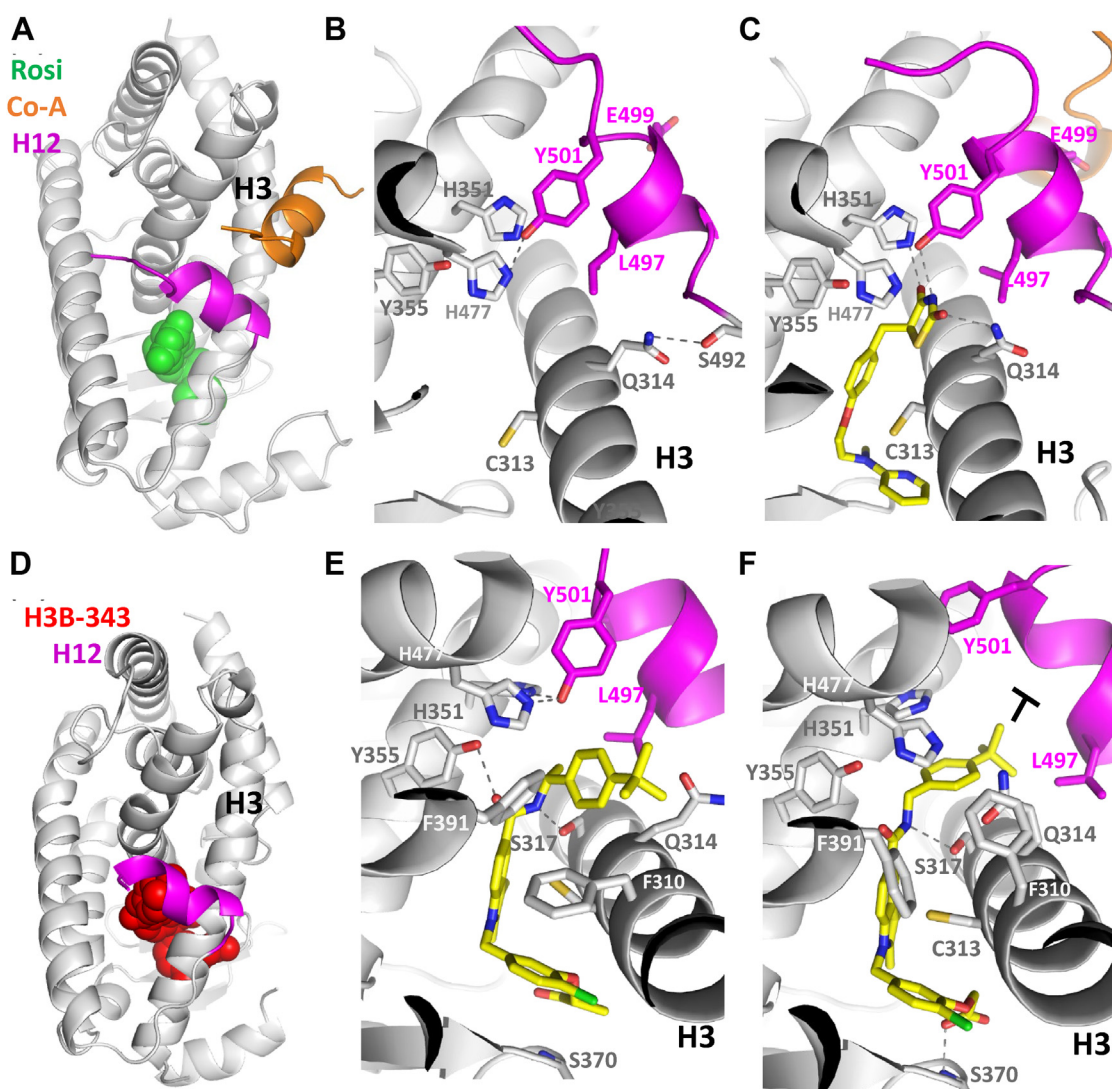


Figure 3. Crystal structures of PPAR γ . A, overall structure bound to rosiglitazone and co-A peptide (PDB code: 2PRG). B, apo structure in agonist conformation (PDB code: 1PRG, monomer A). C, interactions of rosiglitazone with helix 12 (H12) (PDB code: 2PRG). D, overall structure with H3B-343. E, interactions of partial agonist H3B-487 in agonist conformation (monomer A). F, interactions of inverse agonist H3B-343 illustrating the disruption and distortion to H12 with Q314, L497, and Y501 being pushed aside. In all these examples, H12 (magenta) folds over the top of helix 3 outside the ligand-binding pocket. co-A, coactivator; PDB, Protein Data Bank; PPAR γ , peroxisome proliferator-activated receptor gamma.

2.94 Å resolution, again exploiting the known citrate condition with two monomers in the asymmetric unit (Fig. 3, D and F). In this structure, clear electron density is visible for the ligand and, unlike H3B-487, shows identical poses in both monomers (Figs. S6B and S7B). Like H3B-487, H3B-343 also wraps around H3 and makes the same H-bond interaction with S317 (Fig. 3F). Here, the acid substituent forms a key interaction with the backbone amide of S370, which was not apparent in the H3B-487 structure (Fig. 3, E and F). The R-configuration of the stereogenic methyl in H3B-487 may not provide optimal geometry for this H-bond and could explain its weaker binding affinity relative to H3B-343 (Table 1). While the overall pose for these regions of the molecules is similar, the pose of *t*-butyl-phenyl group is flipped (Fig. 3F). The H3B-343 structure shows that the *t*-butyl-phenyl would clash with L497 in the agonist conformation and push it out of the way, thereby subtly shifting the entire helix and disrupting several other

interactions including those with Q314 and Y501, which are now broken (Fig. 3F). This apparent disruption may explain the shift in equilibrium state toward co-R binding. Thus, these subtle changes in structure provide new insights into the remarkable differences in modulatory behavior between SR10221 and its stereoisomer. This mechanism of H12 disruption is similar to that proposed for inverse agonists of PPAR α (27).

To further validate our model for H12 disruption and probe the interactions in the SR10221 series, we designed a few chemical probes to elucidate how different regions of the molecule influence inverse agonism. To probe the importance of the acid, we made the methylester analog, H3B-654, which disrupts this H-bond interaction to S370, and this compound loses significant binding activity as expected (Table 1). As previously described, the *t*-butyl-phenyl group in H3B-343 clashes with L497, leading to the disruption of H12. The

Table 1
Biochemical and cellular data for chemical probes related to SR-10221

ID	Structure	IC ₅₀	Co-A	Co-R IP	Plin2 IP	UMUC9 IP
					R%	
SR-10221		13 ± 3	5.3 ± 2 -11 ± 1%	5.9 ± 2 93 ± 14%	9.3 ± 3 -99 ± 3%	6.6 ± 2 28 ± 4%
H3B-487		220 ± 47	221 ± 20 64 ± 5%	82 ± 27 34 ± 16%	30 ± 1 50 ± 3%	34 ± 3 124 ± 4%
H3B-343		9.2 ± 7	1.5 ± 2 -11 ± 3%	8.8 ± 2 100 ± 3%	11.1 ± 2 -100%	10 ± 5 75 ± 6%
H3B-247		1.3 ± 0.1	1.5 ± 0.4 -14 ± 3%	3.8* -17%	3.0 ± 1 40 ± 3%	NA NA
H3B-654		23,000 ± 13,000	NA NA	1230 ± 420 76 ± 6%	29 ± 3 -71 ± 6%	18 ± 7 79 ± 5%
H3B-110		1.9 ± 0.2	2.2 ± 0.7 65 ± 8%	2.4 ± 1.6 -15 ± 2%	367 ± 8 47 ± 4%	148 ± 9 122 ± 4%

Abbreviations: IP, immunoprecipitation; NA, not applicable.

All the corresponding curves are included in the [supporting information](#). Curve inflection points are given with the %Response, which corresponds to the average response under saturating conditions after normalization to T0070907. IC₅₀ refers to the fluormone assay; co-A and co-R refer to the biochemical peptide recruitment assays; Plin2 refers to the cellular PD assay monitoring expression by qPCR; and UMUC9 is a cellular growth assay where R% <100% corresponds to growth inhibition and R% = 0 corresponds to stasis. In this format, R% >100% corresponds to increased proliferation, as observed for some of the partial agonists and antagonists. Only the inverse agonists have an antiproliferative effect. All data are biological replicates with n = 2 or n = 3 with the exception of the asterisked* singlicate data.

simple removal of the *t*-butyl group in H3B-110 eliminates these disruptive interactions, resulting in a compound that shows partial agonist behavior and presumably stabilizes H12 in the agonist conformation (Table 1, Figs. S2 and S3). Also of note, shifting the *t*-butyl group from the *para* position to the *meta* position in H3B-647 maintains equipotent binding activity in the FRET fluormone assay but eliminates the co-A and co-R recruitment activity in the FRET assays (Table 1 and Fig. S2). While completely inactive by FRET, the compound does show partial agonist activity in the qPCR assay, suggesting the cellular assay provides a more sensitive readout than TR-FRET (Table 1 and Fig. S3).

Crystal structures from the T007 series with co-R peptide

We next endeavored to determine the structural basis for inverse agonism with T007. The activity of this compound was very surprising given its small fragment-like molecular weight when compared with the overall spaciousness of the PPAR γ -binding pocket. We failed to obtain cocrystals of PPAR γ with T007 or JTP-4 using the previously described citrate crystallization conditions, suggesting a totally novel conformation of H12 incompatible with this lattice. We were able to obtain

cocrystals with both T007 and JTP-4 in the presence of co-R peptide at 1.9 and 1.6 Å resolution, respectively, using new crystallization conditions (Fig. 4, A–C) (activity data summarized in Table 2). Here, the crystal packing is consistent with a monomer in the crystal lattice. The electron density shows unambiguously the covalent bond formation between the ligands T007 and JTP-4 with C313 (Fig. S6, C and D). We were also able to clearly resolve the co-R peptide (Fig. 4A). The most remarkable feature of the structure is the rearrangement of the C-terminal H12. Here, H12 reorganizes behind H3 to occupy the majority of the ligand-binding pocket (Fig. 4, A–C). This is achieved, in part, by key stabilizing interactions between the C-terminal most residue Y505 with residues in the ligand-binding pocket: H351, Y355, and K395 (Fig. 4, B and C). In addition, Y505 π -stacks with the pyridine ring of T007, whereas the C-terminal carboxylate forms a key H-bond interaction with the amide nitrogen of T007 (Fig. 4B). Meanwhile, the amide oxygen of T007 forms another key H-bond interaction with Q314 (Fig. 4B). Finally, the nitro group and the pyridine nitrogen form water-mediated interactions. The crystal structure with JTP-4 shows a very similar binding mode (Fig. 4C). The JTP-4 compound is very flat, and the interactions are similar to T007, except the additional

Inverse agonists inhibit PPAR γ through distinct mechanisms

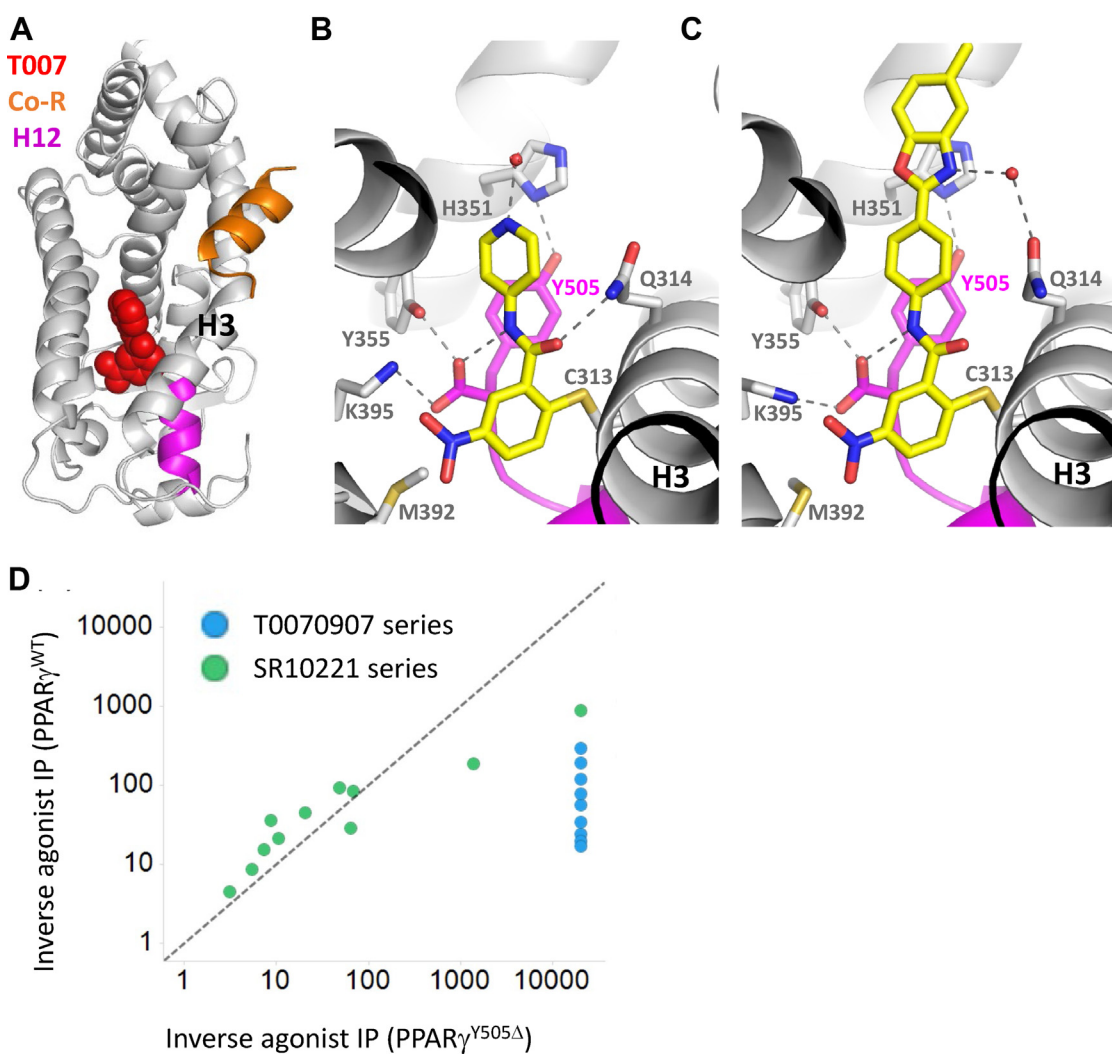


Figure 4. T007 series bound to PPAR γ . H12 undergoes a dramatic conformational change folding underneath H3 and entering the ligand-binding pocket. *A*, overall structure with T007 and co-R peptide. *B*, interactions formed by T007 in the binding pocket. Y505 makes key interaction with T007 amide. *C*, interactions formed with JTP-4 are similar to T007 with additional stacking interaction with H351. *D*, Y505 is critical for inverse agonism across T007 series. Covalent T007 series completely lose their ability to induce inverse agonism in the absence of Y505. The inverse agonist activity of the SR10221 series is largely unaffected by the Y505D mutation, highlighting the difference in mechanism from T007. co-R, corepressor; H3, helix 3; H12, helix 12; JTP-4, JTP-4, 426467; PPAR γ , peroxisome proliferator-activated receptor gamma; T007, T0070907.

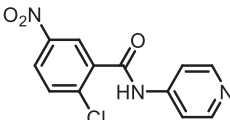
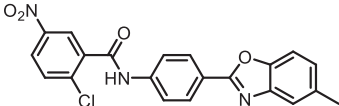
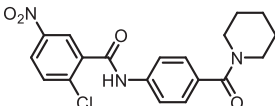
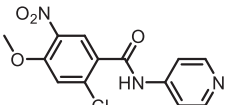
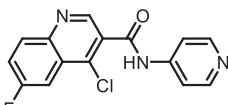
benzoxazole group forms additional stabilizing π - π interactions with H351 (Fig. 4C). Importantly, these structures clearly reveal the structural basis for inverse agonism. Because the co-R motif contains an extra helical turn relative to co-A, H12 must be displaced to create enough room for co-R binding. The covalent inverse agonists T007 and JTP-4 accomplish this beautifully by stabilizing the conformational reorganization of H12 inside the binding pocket through direct interaction with Y505, thereby revealing a completely unhindered binding site for co-R.

To further characterize the significance of the interactions observed in the crystal structures, we examined some of the key interactions with mutagenesis. The most striking difference in conformation between the two inverse agonist-bound crystal structures is the position of H12. In the T007 series, the C-terminal Y505 carboxylate makes critical interactions with the ligand and is important for tethering H12 inside the ligand-binding pocket. The SR10221 series, in contrast, shows no

interaction with Y505. We therefore made a PPAR $\gamma^{Y505\Delta}$ construct and validated it using our FRET fluormone binding assay to show that agonists and inverse agonists alike are able to bind in the ligand-binding pocket. A key difference in behavior was observed in the FRET inverse agonist assay. While the SR10221 series of compounds still recruit co-R peptide, the mutation completely abolishes co-R recruitment for the T007 series (Fig. 4D). These data clearly indicate the importance of Y505 in anchoring H12 in the ligand-binding pocket to reveal the co-R binding site for T007 series activity.

We investigated additional interactions in the T007 series by generating a series of chemical probes. Both the T007 and JTP-4 crystal structures show that the *para*-nitro-chloro-phenyl ring is buried in the pocket, and we found that modification to this ring with O-methoxy is not compatible with inverse agonism but retains antagonist activity (Table 2 and Fig. S2). We also explored different kinds of electrophiles, such as H3B-766. This compound had exquisite antagonist potency but

Table 2
Biochemical and cellular data for chemical probes related to T0070907

ID	Structure	IC ₅₀	Co-A IP	Co-R IP	Plin2 IP	UMUC9 IP
					R%	
T007		9.9 ± 1.3	4.4 ± 0.9 -10 ± 0.6%	12 ± 0.4 98 ± 6%	15* -94%	14 ± 3 40 ± 2%
JTP-4		90 ± 21	23 ± 14 -15 ± 3%	72 ± 6 93 ± 6%	17 ± 2 -82 ± 4%	12 ± 3 24 ± 10%
H3B-822		10*	32 ± 20 10 ± 1%	NA 10 ± 4%	21 ± 3 40 ± 4%	24 ± 5 117 ± 4%
H3B-951		343*	211 10.2%	NA 0%	345* 32%	332 ± 20 110 ± 5%
H3B-766		7*	9.6 ± 0.4 9.1 ± 2%	7.2 ± 1 -13 ± 1.5%	2515 ± 30 64 ± 5%	54 ± 11 125 ± 10%

Abbreviations: IP, immunoprecipitation; NA, not applicable. See Table 1 for definitions of assays and assay parameters.

showed no activity in the co-A or co-R recruitment assays and showed partial agonism by qPCR (Table 2 and Figs. S2–S4). On the other side of the pocket, the pyridine group is directed outward toward solvent and tolerates a wider variety of substituents, as exemplified by JTP-4. However, a planar configuration for these groups is preferred. Groups that twist out of plane clash with H351 and lose activity in the inverse agonist assay, whereas retaining activity in the fluoromone displacement assays. These compounds, such as H3B-822, are pure antagonists in the FRET assays (Table 1 and Fig. S2).

Discussion

Repression of PPAR γ signaling is emerging as a possible therapeutic intervention strategy in bladder cancer (12, 13). The data presented here extend upon previous work demonstrating that repression of PPAR γ activity depends on the recruitment of co-R complexes NCOR and SMRT (13). Such compounds that bind receptor and promote the recruitment of co-R complexes are so-called inverse agonists, because they repress gene expression below the basal state of the aporeceptor. These compounds are distinct from antagonists: compounds that bind PPAR γ but do not promote recruitment of co-A or co-R. Our results signify that at least two series of compounds, exemplified by T007 and SR10221, enhance binding to co-Rs leading to repression of PPAR γ -mediated gene expression below their basal state. Our results demonstrate that these compounds also induce phenotypic growth suppression in cell lines that are PPAR γ^{high} but not in the PPAR γ^{low} line. We also show that structurally related

compounds that are antagonists act as silent ligands in biochemical co-A and co-R recruitment assays and as weak partial agonists in qPCR assays. Together, these data are consistent with inverse agonists being the appropriate therapeutic modality to repress PPAR γ signaling.

To understand the structural basis for inverse agonism, we determined crystal structures of two covalent inverse agonists T007 and JTP-4 as well as the noncovalent inverse agonist H3B-343, which is structurally related to SR10221. Prototypic crystal structures of PPAR γ show that co-A binding is favored because H12 forms a key stabilizing H-bond interaction with a helical turn in co-A (Fig. 3, B and C). In this conformation, co-R binding is less favored because it contains an additional helical turn that would clash with H12. Therefore, to promote co-R binding, H12 needs to relocate, which both eliminates this H-bond interaction with co-A and creates the necessary room for co-R. Our cocrystal structures with co-R peptide show that both T007 and JTP-4 induce a dramatic rearrangement of H12, forming key interactions between the amide pharmacophore and the C-terminal carboxylate of Y505. This stabilizing interaction tethers H12 within the ligand-binding pocket and reveals a large docking interface for co-R that was otherwise partially masked by H12. These results extend upon and complement recent reports showing a similar conformational rearrangement in H12 upon binding to T007 (28).

We further validate the importance of Y505 by making the single amino acid deletion mutant and showing that T007 and JTP-4 completely lose their inverse agonist activity in this mutant setting. Moreover, we characterize additional chemical

Inverse agonists inhibit PPAR γ through distinct mechanisms

probes from this series. In particular, modifications to the *para*-nitro-chloro-phenyl ring lose inverse agonist activity because this side is deeply buried in the inverse agonist binding mode. For example, the modified compound H3B-766 retains a covalent mechanism of action and is a very potent antagonist in our biochemical assays, but it loses all inverse agonist activities. The crystal structure with T007 also shows that the pyridine ring is more solvent exposed, which explains why JTP-4 is also a potent inverse agonist. JTP-4 picks up additional π - π stacking interactions, and indeed, our studies have shown that numerous groups are tolerated at the pyridine nitrogen position. However, certain groups are not tolerated at this position, and it appears that the flat coplanar ring system is important because compounds that twist out of plane, such as the covalent compound H3B-822, lose inverse agonist activity but retain antagonist activity. We posit that this antagonist is not able to induce the inverse agonist conformation, possibly because of these clashing interactions. Indeed, H3B-766 and H3B-822 are critical tools from this series for helping to understand the biological difference between antagonism and inverse agonism. Our data show that neither of these antagonists repress PPAR γ gene expression by qPCR and surprisingly show some weak partial agonism in this assay format.

We also investigated the noncovalent SR10221 compound. The first reported indole-based modulator of PPAR γ was GSK538 (29). This compound is a potent nanomolar binder with partial agonist activity (29). This scaffold formed the basis for the discovery of the antagonist SR1664 (30) and ultimately the inverse agonist SR10221 (23). The structure-based design hypothesis was to anchor a potent scaffold in the pocket and extend from this indole core to disrupt H12 as had been reported with other NHRs such as estrogen receptor alpha and PPAR α (27). Despite the apparent success of this strategy, thus far, a crystal structure of an inverse agonist from this series has not been reported. We were unable to cocrystallize SR10221, but we were able to show that a nonstereogenic analog H3B-343 shows nearly identical properties in biochemical and cellular assays, and we were able to obtain cocrystals with this compound. Our crystal structure shows the same binding mode for the indole core as previously shown for the partial agonist GSK538 and weak antagonist SR1664. However, our results with the potent H3B-343 show that the *t*-butyl-phenyl ring flips into a completely different conformation, clearly pushing against key side-chain residues to destabilize the H12 agonist conformation. We believe that this ligand conformation and the consequences to H12 stability capture more accurately the structural basis for inverse agonist activity in this series. To further validate this model, we examined a few close analogs of H3B-343. These include an analog that lacks the *t*-butyl group and becomes an agonist, an analog shifting the *t*-butyl from the *para* to the *meta* position, which leads to antagonism only, and finally, the stereoisomer of SR10221, H3B-487. The conformation of the *t*-butyl-phenyl ring in H3B-487 overlays very well with those in the GSK538 and SR1664 structures, indicating that this ligand-binding pose represents a partial agonist conformation.

In summary, our results provide a broad contextual and mechanistic understanding for two distinct series of compounds known to induce inverse agonism in PPAR γ . To fully suppress PPAR γ activity, recruitment of co-Rs appears to be necessary. Our assays also provide a means to classify the continuum of compound behavior from partial inverse agonism to super inverse agonism, which may be helpful for further subclassifying compounds. Finally, these data may form the basis for further structure-based drug design efforts and future medicinal chemistry efforts to improve the properties of these compounds to enable *in vivo* studies.

Experimental procedures

Protein expression and purification

The constructs His₆-TEV-PPAR γ -(234–505), His₆-TEV-PPAR γ -(234–504), and the RXR α ^{WT}-PPAR γ and RXR α ^{S427F}-PPAR γ heterodimer complexes were expressed and purified as previously described (12). For crystallization, we also removed the hexahistidine tag using His₆-TEV protease, removed residual protease by subtractive nickel–nitrilotriacetic acid, and polished the final PPAR γ protein by size-exclusion chromatography. The protein was concentrated to \sim 20 mg ml⁻¹ in 20 mM Tris, pH 8.0, 100 mM NaCl, and 1 mM Tris(2-carboxyethyl)phosphine and stored at -80 °C.

ITC

ITC measurements were performed with an ITC200 (Malvern Instruments). All proteins were dialyzed into assay buffer (25 mM Tris [pH 8.0] and 100 mM NaCl) prior to measurement. The sequence for co-A peptide PGC1 α was Ac-¹³⁸AEEPSSLKLLAPA¹⁵²-amide and for co-R peptide SMRT2 (also known as NCOR2) was Ac-²³⁴⁶TNMGLEAIRKALMGKYDQWEE²³⁶⁷-amide. For PGC1 α titrations with heterodimer, the cell was loaded with either 20 μ M mutant or 40 μ M WT heterodimer, and the syringe was loaded with 300 μ M peptide or 600 μ M peptide for the mutant and WT, respectively. For SMRT2 titrations, the cell was loaded with either 50 μ M mutant or 40 μ M WT heterodimer and the syringe with 600 μ M or 800 μ M peptide for mutant and WT, respectively. All experiments were run at 23 °C. Titration experiments consisted of twelve 3 μ l injections with 120 s of equilibration between injections. The enthalpy peaks were integrated and fit to a 1:1 binding model using Origin software (OriginLab; <https://www.originlab.com/>). RXR α does not interact with PGC1 α in the absence of ligand (data not shown), so all binding to the heterodimer was attributed to interaction with PPAR γ . The measured 1:1 stoichiometry of interaction supports this interpretation.

Mini peptide array experiments

For peptide array experiments, His₆-PPAR γ -(234–505) was diluted to 10 nM in assay buffer (50 mM potassium chloride, 50 mM Hepes [pH 7.4], 2 mM DTT, 0.1 mg/ml bovine gamma-globulin, and 0.001% Pluronic F-127). Protein (5 μ l) was then added to a 384-well (Corning 3820) assay ready plate containing 22 replicates of 2 μ M compound (columns 1–22) delivered by an

acoustic dispenser. Column 23 contained 1 μ M rosiglitazone, and column 24 contained 500 nM T007 as 100% positive and -100% negative controls, respectively. After a 1 h incubation with compound, fluorescently labeled peptides (Table S1) were added to final concentration of 200 nM (columns 1–21) and FITC-Biotin (column 22) as a nonspecific binding control. Immediately afterward, anti-6xHis-Terbium labeled antibody was added to each well with a combi liquid handler (Thermo). Plates were covered, centrifuged, and incubated for an additional hour. The TR-FRET data were recorded with an Envision plate reader (PerkinElmer), using settings recommended by Thermo Fisher. The raw signal was then plotted in SpotFire (TIBCO; <https://www.tibco.com/products/tibco-spotfire>).

Co-A and co-R peptide recruitment to PPAR γ (TR-FRET)

For the co-A and co-R recruitment assays, protein and buffer was the same as for the peptide array experiments and added to a 384-well (Corning 3820) assay ready plate containing compounds (columns 1–22) delivered by an acoustic dispenser. For the high-throughput screen, compounds were tested at a single concentration of 40 μ M. Otherwise, for routine testing, compounds were arrayed in 11 point, half log, dilution series with an initial top concentration of 40 μ M. Column 23 contained an identical volume of dimethyl sulfoxide (DMSO) for the negative control, and column 24 contained 500 nM of T007 or rosiglitazone for the positive controls of the co-R and co-A assays, respectively. After 1 h of room temperature incubation with the compound, detection solution was added consisting of 5 nM anti-6xHis-Terbium antibody (CisBio) and 200 nM fluorescently labeled SMRT-ID2 co-R peptide or TRAP220-DRIP2 co-A peptide (Table S1). After an additional hour of incubation, TR-FRET data were recorded as before. The values from the positive and negative controls' recruitment of FITC-peptide were used to normalize the TR-FRET signal to percent response and to calculate an assay Z prime. Dose-response data were analyzed in SpotFire. Data quality was assessed on several levels. During routine compound profiling, columns 23 and 24 were used to calculate a Z' to evaluate data quality at the plate level, and any plate with a Z' < 0.65 was rejected. In addition, every weekly screening run included repeat control compounds, which were used to assess reproducibility plate to plate and week to week. Finally, for test compounds, replicates were examined for reproducibility with n = 2 or n = 3 whenever possible.

Fluormone assays (TR-FRET)

For the fluormone competition assay, conditions were identical to the peptide recruitment assays; however, during detection, 20 nM Pan-PPAR Fluormone green ligand (Thermo Fisher) was used in place of the peptide. This assay measures binding competition between compound and the fluorescent ligand and is agnostic to the modality (agonist or inverse agonist). Competition with fluormone binding results in a loss of TR-FRET signal relative to the DMSO control. The negative and positive controls were comprised of the same volumes and concentrations of DMSO and T007 used for the peptide recruitment assays.

Dose-response data were analyzed in SpotFire. Data were quality controlled (QC'd) as described previously.

Nanostring assay

About 5637 cells were treated in triplicate with compounds as indicated for 48 h followed by RNA extraction using the Taqman Cells-to-CT kit by Thermo Fisher Scientific. The RNA sample was quantified by NanoDrop (Thermo Fisher Scientific). All assessed samples had a minimum yield of 400 ng RNA. Direct mRNA expression levels of the samples were measured using a custom nCounter gene expression panel (NanoString Technologies) following the manufacturer's recommendations.

qPCR assay

UM-UC-9 cells were obtained from SIGMA and cultured in Eagle's minimum essential medium (Earle's balanced salt solution) + 2 mM glutamine + 1% nonessential amino acids + 10% fetal bovine serum. For qPCR assays, 500 cells were seeded in each well of a 384-well plate 1 day before compound addition. Dose response was measured in 11-point serial dilutions with a top dose of 10 μ M. The percentage of DMSO was controlled throughout, and a DMSO-only control was included. Forty-eight hours after dosing, cells were lysed. About 25 nl was used for RT-qPCR. RT-qPCRs were prepared using TaqMan RNA-to-CT 1-step kit (Life Technologies), Plin2 junction (forward: ACTCTCTTCCGCATCGCTGT; reverse: CCGACGGGTTTCCGATCCAA; probe: CTGTTGGGCTCGCGGTTG) and Ftz (forward: TGGCATCAGATTGCAAAGAC; reverse: ACGCCGGGTGATGTATCTAT; probe: CGAAACGCACCCGTCAGACG) mRNA primer-probe sets. GraphPad Prism (Dotmatics; <https://www.graphpad.com/>) was used for nonlinear regression curve fitting of the gene expression level and normalized to the untreated/DMSO sample. Data were plotted using SpotFire. Data were QC'd as described previously.

Viability assay

UM-UC-9 and UM-UC-3 cells were obtained from SIGMA and expanded in DMEM supplemented with 10% fetal bovine serum, 25 mM glucose, 4.0 mM L-glutamine, 2.0 mM GlutaMAX, 1.0 mM pyruvate, and 1.0% nonessential amino acids in a 95% humidified incubator at 37 °C with 5% CO₂. Frozen cell banks were then prepared during their exponential growth stage to enable reproducible biweekly assay support at a consistent cell passage. For routine assays, a vial of frozen cells was recovered, and 500 cells were dispensed (using Thermo Combi) into each well of a 384-well plate (Corning 3571) that was pretreated with acoustically dispensed compounds (50 nl per well) in half log 11-point dose response with a top final concentration of 10 μ M (columns 1–22). Column 23 contained DMSO as a negative control, and column 24 contained 1 μ M bortezomib as a positive control for cell death. Freshly seeded plates were incubated at 37 °C, 5% CO₂, and 95% relative humidity (STX110; Liconic). After 7 days, a cell proliferation assay was performed using CellTiter-Glo, and the

Inverse agonists inhibit PPAR γ through distinct mechanisms

plates were read on an EnVision. Luminescence values from each treatment were normalized to the average value of the respective DMSO control. The dose–response curve plots were generated in SpotFire, and GI₅₀s were calculated from nonlinear regression analysis. Data were QC'd as described previously.

Crystallization and structure determination

Numerous PPAR γ cocrystal structures have been determined from the well-known sodium citrate condition (26). We also obtained cocrystals from this condition with the SR10221 analogs H3B-343 and H3B-487 by seeding techniques in the hanging drop format over reservoirs containing 0.9 to 1.2 M sodium citrate and 100 mM Tris (pH 8.0). Crystals with H3B-343 and H3B-487 diffracted to 2.94 Å and 2.48 Å resolution, respectively, and the structures were solved by molecular replacement (Table S2). For T007 and JTP-4, we were unable to obtain cocrystals from any previously reported conditions. Therefore, we performed sparse matrix screens in the presence and absence of co-R peptide to find new crystallization conditions. We obtained crystals using a 2:2:1 M ratio of T007:NCOR peptide:PPAR γ from a well solution containing 1.8 to 2.2 M (NH₃)₂SO₄, 0.2 M Li₂SO₄, and 100 mM CAPS (pH 9.5). Crystals with T007 and JTP-4 diffracted to 1.9 and 1.6 Å resolution, respectively, and the structures were solved by molecular replacement (Table S2).

Data availability

Coordinates have been deposited in the Protein Data Bank with codes 8DKN, 8DKV, 8DSZ, and 8DSY.

Supporting information—This article contains supporting information.

Author contributions—P. F., P. Z., M. K., and N. A. L. conceptualization; S. I., C. K., and C. F. methodology; S. I., C. K., C. F., J. T., P. G., D. B., A. S. W., A. A. D., M. O., J. Y., J. L., and N. A. L. investigation; N. A. L. writing—original draft; N. A. L. visualization; L. M., S. R., P. F., P. Z., M. K., and N. A. L. supervision.

Conflict of interest—The main authors are employees of H3 Biomedicine. The authors declare that they have no conflicts of interest with the contents of this article.

Abbreviations—The abbreviations used are: co-A, coactivator; co-R, corepressor; DMSO, dimethyl sulfoxide; H3, helix 3; H12, helix 12; ITC, isothermal titration calorimetry; JTP-4, JTP-426467; LBD, ligand-binding domain; MIBC, muscle-invasive bladder cancer; NHR, nuclear hormone receptor; PPAR γ , peroxisome proliferator-activated receptor gamma; QC'd, quality controlled; qPCR, quantitative PCR; T007, T0070907; TR-FRET, time-resolved FRET.

References

1. Miller, R. L., Siegel, K. D., Lin, A., Mariotto, A. B., Kramer, J. L., Rowland, J. H., *et al.* (2016) Cancer treatment and survivorship statistics, 2016. *CA Cancer J. Clin.* **66**, 271–289
2. Witjes, J. A., Compérat, E., Cowan, N. C., De Santis, M., Gakis, G., Lebre, T., *et al.* (2014) EAU guidelines on muscle-invasive and metastatic bladder cancer: summary of the 2013 guidelines. *Eur. Urol.* **65**, 778–792
3. von der Maase, H., Sengelov, L., Roberts, J. T., Ricci, S., Dogliotti, L., Oliver, T., *et al.* (2005) Long-term survival results of a randomized trial comparing gemcitabine plus cisplatin, with methotrexate, vinblastine, doxorubicin, plus cisplatin in patients with bladder cancer. *J. Clin. Oncol.* **23**, 4602–4608
4. Felsenstein, K. M., and Theodorescu, D. (2018) Precision medicine for urothelial bladder cancer: update on tumour genomics and immunotherapy. *Nat. Rev. Urol.* **15**, 92–111
5. Lawrence, M. S., Stojanov, P., Polak, P., Kryukov, G. V., Cibulskis, K., Sivachenko, A., *et al.* (2013) Mutational heterogeneity in cancer and the search for new cancer-associated genes. *Nature* **499**, 214–218
6. Comprehensive molecular characterization of urothelial bladder carcinoma. *Nature* **507**, (2014), 315–322
7. Robertson, A. G., Kim, J., Al-Ahmadie, H., Bellmunt, J., Guo, G., Cherniack, A. D., *et al.* (2017) Comprehensive molecular characterization of muscle-invasive bladder cancer. *Cell* **171**, 540–556.e25
8. Audenet, F., Attalla, K., and Sfakianos, J. P. (2018) The evolution of bladder cancer genomics: what have we learned and how can we use it? *Urol. Oncol.* **36**, 313–320
9. Rodriguez-Vida, A., Lerner, S. P., and Bellmunt, J. (2018) The cancer genome atlas project in bladder cancer. *Cancer Treat. Res.* **175**, 259–271
10. Warrick, J. I., Walter, V., Yamashita, H., Chung, E., Shuman, L., Amponsa, V. O., *et al.* (2016) FOXA1, GATA3 and PPAR cooperate to drive luminal subtype in bladder cancer: a molecular analysis of established human cell lines. *Sci. Rep.* **6**, 38531
11. Rosenberg, J. E., Hoffman-Censits, J., Powles, T., van der Heijden, M. S., Balar, A. V., Necchi, A., *et al.* (2016) Atezolizumab in patients with locally advanced and metastatic urothelial carcinoma who have progressed following treatment with platinum-based chemotherapy: a single-arm, multicentre, phase 2 trial. *Lancet* **387**, 1909–1920
12. Korpala, M., Puyang, X., Jeremy Wu, Z., Seiler, R., Furman, C., Oo, H. Z., *et al.* (2017) Evasion of immunosurveillance by genomic alterations of PPAR γ /RXR α in bladder cancer. *Nat. Commun.* **8**, 103
13. Goldstein, J. T., Berger, A. C., Shih, J., Duke, F. F., Furst, L., Kwiatkowski, D. J., *et al.* (2017) Genomic activation of PPARG reveals a candidate therapeutic axis in bladder cancer. *Cancer Res.* **77**, 6987–6998
14. Halstead, A. M., Kapadia, C. D., Bolzenius, J., Chu, C. E., Schriefer, A., Wartman, L. D., *et al.* (2017) Bladder-cancer-associated mutations in RXRA activate peroxisome proliferator-activated receptors to drive urothelial proliferation. *Elife* **6**, e30862
15. Sweis, R. F., Spranger, S., Bao, R., Paner, G. P., Stadler, W. M., Steinberg, G., *et al.* (2016) Molecular drivers of the non-T-cell-inflamed tumor microenvironment in urothelial bladder cancer. *Cancer Immunol. Res.* **4**, 563–568
16. Davidson, M. A., Mattison, D. R., Azoulay, L., and Krewski, D. (2018) Thiazolidinedione drugs in the treatment of type 2 diabetes mellitus: past, present and future. *Crit. Rev. Toxicol.* **48**, 52–108
17. Mohanty, P., Aljada, A., Ghanim, H., Hofmeyer, D., Tripathy, D., Syed, T., *et al.* (2004) Evidence for a potent antiinflammatory effect of rosiglitazone. *J. Clin. Endocrinol. Metab.* **89**, 2728–2735
18. Hu, X., and Lazar, M. A. (1999) The CoRNR motif controls the recruitment of corepressors by nuclear hormone receptors. *Nature* **402**, 93–96
19. Gampe, R. T., Jr., Montana, V. G., Lambert, M. H., Miller, A. B., Bledsoe, R. K., Milburn, M. V., *et al.* (2000) Asymmetry in the PPARgamma/RXRalpha crystal structure reveals the molecular basis of heterodimerization among nuclear receptors. *Mol. Cell* **5**, 545–555
20. Rochel, N., Krucker, C., Coutos-Thévenot, L., Osz, J., Zhang, R., Guyon, E., *et al.* (2019) Recurrent activating mutations of PPARgamma associated with luminal bladder tumors. *Nat. Commun.* **10**, 253
21. LeeLee, G., Elwood, F., McNally, J., Weiszmann, J., Lindstrom, M., Amaral, K., *et al.* (2002) T0070907, a selective ligand for peroxisome

- proliferator-activated receptor gamma, functions as an antagonist of biochemical and cellular activities. *J. Biol. Chem.* **277**, 19649–19657
22. Nishiu, J., Ito, M., Ishida, Y., Kakutani, M., Shibata, T., Matsushita, M., *et al.* (2006) JTP-426467 acts as a selective antagonist for peroxisome proliferator-activated receptor gamma *in vitro* and *in vivo*. *Diabetes Obes. Metab.* **8**, 508–516
 23. Marciano, D. P., Kuruvilla, D. S., Boregowda, S. V., Asteian, A., Hughes, T. S., Garcia-Ordenez, R., *et al.* (2015) Pharmacological repression of PPARgamma promotes osteogenesis. *Nat. Commun.* **6**, 7443
 24. Itoh, T., Fairall, L., Amin, K., Inaba, Y., Szanto, A., Balint, B. L., *et al.* (2008) Structural basis for the activation of PPARgamma by oxidized fatty acids. *Nat. Struct. Mol. Biol.* **15**, 924–931
 25. Brust, R., Shang, J., Fuhrmann, J., Mosure, S. A., Bass, J., Cano, A., *et al.* (2018) A structural mechanism for directing corepressor-selective inverse agonism of PPARgamma. *Nat. Commun.* **9**, 4687
 26. Nolte, R. T., Wisely, G. B., Westin, S., Cobb, J. E., Lambert, M. H., Kurokawa, R., *et al.* (1998) Ligand binding and co-activator assembly of the peroxisome proliferator-activated receptor-gamma. *Nature* **395**, 137–143
 27. Xu, H. E., Stanley, T. B., Montana, V. G., Lambert, M. H., Shearer, B. G., Cobb, J. E., *et al.* (2002) Structural basis for antagonist-mediated recruitment of nuclear co-repressors by PPARalpha. *Nature* **415**, 813–817
 28. Shang, J., Mosure, S. A., Zheng, J., Brust, R., Bass, J., Nichols, A., *et al.* (2020) A molecular switch regulating transcriptional repression and activation of PPARgamma. *Nat. Commun.* **11**, 956
 29. Lamotte, Y., Martres, P., Faucher, N., Laroze, A., Grillot, D., Ancellin, N., *et al.* (2010) Synthesis and biological activities of novel indole derivatives as potent and selective PPARgamma modulators. *Bioorg. Med. Chem. Lett.* **20**, 1399–1404
 30. Choi, J. H., Banks, A. S., Kamenecka, T. M., Busby, S. A., Chalmers, M. J., Kumar, N., *et al.* (2011) Antidiabetic actions of a non-agonist PPARgamma ligand blocking Cdk5-mediated phosphorylation. *Nature* **477**, 477–481